

I. Fracturing procedure and terminal surfaces in SrTiO₃

The Laue-aligned crystals were firmly anchored by partially burying and gluing them in a trench in the sample-holder. A top-post was then glued to the upper exposed surface. The *in-situ* low-temperature fractures were obtained by applying a rapid and strong force to the top-post with a rigid wobble-stick.

The observation of dispersing bands of narrow line-shapes in the ARPES spectra means that the terraces in the area probed by the photon beam are atomically flat, a necessary condition to obtain good momentum resolution. Recent scanning-tunneling microscopy experiments have reported atomically-flat terraces of sub-micron lateral sizes when cleaving at $T < 50$ K, with the terminations assigned as TiO₂ being smoother than the terminations assigned as SrO [SR1, SR2]. It is thus very probable that, within the area illuminated by the photon beam, both TiO₂- and SrO-terminated terraces are present. Our experiment cannot tell whether the observed bands come from one or both types of terminations. However, the narrow line-widths and the fact that the bands have a clear symmetry ordering imply that either the subbands of both terminations are very similar, or that only one type of termination contributes to the measured electronic structure. In this latter case, it would be probably the smoother TiO₂ termination, which is also the terminal surface necessary to obtain a 2DEG in the LaAlO₃/SrTiO₃ heterostructures [SR3].

As we show later, our first-principles calculations also demonstrate that, in the presence of oxygen vacancies, both surface terminations yield subband structures that are qualitatively similar and compatible with the experimental observations.

II. Transport measurements and bulk carrier concentrations

The electrical transport properties of the samples of this study were characterized by *dc* measurements at room temperature (non-doped sample) and down to 3 K (low-doped and highly-doped samples). For the non-doped and low-doped regimes, we characterized samples prepared under conditions identical to the samples used for the ARPES experiments. For the highly-doped regime, the sample studied by transport and the sample measured by ARPES were two pieces cut off the same original sample.

All the samples are about $5 \times 5 \times 0.5$ mm³. The samples were measured with four

Sample	ρ (Ω cm)		n_{3D} (cm^{-3})		μ_H ($\text{cm}^2\text{V}^{-1}\text{s}^{-1}$)	
	295 K	3 K	295 K	3 K	295 K	3 K
low-doped	0.29	$3.45 \cdot 10^{-4}$	$(3.3 \pm 0.3) \cdot 10^{18}$	$(3.02 \pm 0.02) \cdot 10^{18}$	7	2320
highly-doped	$1.14 \cdot 10^{-2}$	$2.91 \cdot 10^{-4}$	$(7.7 \pm 0.1) \cdot 10^{19}$	$(7.1 \pm 0.2) \cdot 10^{19}$	7.1	303

TABLE I: Main electrical transport properties at room temperature and at 3 K (resistivity, Hall carrier density and Hall mobility).

contacts on the four corners of one large face of the parallelepiped. The contacts are made by aluminum bonding on deposited aluminum pads for the highly-doped sample and by silver epoxy (dried at room temperature) for the low-doped sample. The resistivity ρ is then given by $\rho = \frac{\pi d}{\ln(2)} \frac{R_1 + R_2}{2} f$, where d is the thickness of the parallelepiped, R_1 and R_2 are the resistances with the current applied on two perpendicular side (opposite sides give the same value), and f is a function of the ratio R_1/R_2 which is very close to one in our case (van der Pauw) [SR4]. Similarly, the Hall resistance is determined by $R_H = \frac{d}{B} \Delta R$, where ΔR is the resistance change measured as the magnetic field B is increased. This resistance is measured with the current flowing along a diagonal of the large face. (The same result is found using the two diagonals, within the error margins). The carrier density is then estimated by $n_{3D} = R_H^{-1}/e$, where e is the electron charge, and is found to be nearly temperature independent.

Table I displays the measured quantities at room temperature and at 3 K for the low-doped and highly-doped samples. Figure 1 shows the resistivity and the mobility as extracted by the above procedure. Two characteristic Hall measurements are also shown. Comparing the low temperature mobility with the general mobility versus doping diagram for doped SrTiO₃ by oxygen reduction [SR5, SR6], a perfect agreement is found.

For the non-doped sample, the resistance at room temperature measured at the above geometry was larger than $100 \text{ G}\Omega$, which made impractical to measure the low-temperature data. Assuming that $\rho \times n_{3D}$ is roughly independent of doping, which holds for the low-doped and highly-doped samples (see table I), we deduce that the carrier density for the non-doped sample is $n_{3D} \lesssim 10^{13} \text{ cm}^{-3}$.

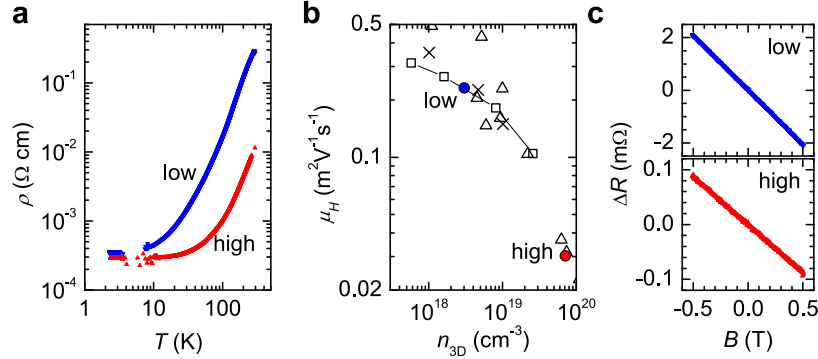


Figure SF 1: **Transport properties of the low- and highly-doped samples.** **a** Resistivity as a function of temperature. **b** Mobility as a function of the bulk carrier density for oxygen-reduced SrTiO_3 at low temperature. The samples of this study are the colored circle ($T = 3 \text{ K}$), other samples are from Ref. SR5 (\times $T = 4.2 \text{ K}$ and \square $T = 2 \text{ K}$) and SR6 (\triangle $T = 4.2 \text{ K}$). **c** Hall resistance as a function of the magnetic field at $T = 3 \text{ K}$ for the low-doped (top panel) and highly-doped (bottom panel) samples.

III. Photon energy dependence of the electronic subbands at the surface of SrTiO_3

Figure SF 2 presents data obtained at normal emission as a function of photon energy. The data were collected using linear horizontal (LH) light polarization (polarization vector in the xz plane), and detection along x [horizontal (H) slits] in the sample's xz -plane, which in this geometry also coincides with the light incidence plane. The final electron state has to be even with respect to the sample's mirror plane to be detected by the analyzer (the xz -plane in this case) –otherwise the electron wavefunction would be zero in this plane. Hence, the dipole-transition selection rules imply that the initial state and the dipole operator (equivalently, the polarization vector) must have the same symmetry with respect to the mirror plane [SR9, SR10]. In the geometry of figure SF 2, the light polarization is even under reflection on the xz plane. Thus, only initial states of even parity with respect to this plane can be detected. Hence, only the upper d_{xz} -like band, which is furthermore *light* along x , is observed in this geometry (experimentally, the lower d_{xz} -like band has a very weak intensity in this geometry).

As observed in Fig. SF 2(c, d), the upper d_{xz} -like band does not disperse as a function of photon energy, or equivalently as a function of k_z , confirming its 2D surface-like character. However, it presents a marked intensity modulation as a function of photon energy, a

behaviour also observed in surface states and quantum well states of simple metallic systems [SR7, SR8]. Thus, for instance, while the band is clearly seen at $h\nu = 30$ eV, its intensity is very weak around $h\nu = 47$ eV, where the rest of our experiments were performed. As explained in the main text, and also discussed below, at this photon energy the d_{xz} -like bands and the other subbands are distinctly observed in other Brillouin zones and other polarization/slits geometries.

IV. Intensity modulations of the electronic subbands with emission angle and photon polarization

Fig. SF 3 shows the energy-momentum intensity maps for cuts at three points in reciprocal space labeled as A, B and C. The spectra at points B and C were already discussed in the main text, and are again shown here for clarity and completeness in the discussion.

The three points A, B and C correspond to different positions along the (001) (or k_z) axis and different emission angles, as represented in Fig. SF 3(a) [SR10, SR12], such that $\Gamma_{002}A = 0.7(\frac{\pi}{a}) = 0.56 \text{ \AA}^{-1}$, $\Gamma_{012}B = 0.25(\frac{\pi}{a}) = 0.2 \text{ \AA}^{-1}$ and $\Gamma_{112}C \approx -\Gamma_{012}B$ (a is the cubic SrTiO₃ lattice parameter). All the spectra in this figure were measured at $h\nu = 47$ eV with LH light polarization and detection along y [vertical (V) slits], as schematically shown in Fig. SF 3(b). At normal emission (point A), the detection plane coincides with the sample's yz -plane. Exactly at Γ , as explained in the previous section, the only symmetry-allowed states are d_{xz} -like, which have however a very weak intensity at this photon energy. Note that in this case the polarization vector has components both along the x and z directions, the first being odd with respect to the detection plane, and the second even with respect to the same plane. Thus, away from Γ , at emission along the yz -plane, both d_{xy} -like bands (odd with respect to the yz -plane) and d_{yz} -like bands (even with respect to the same plane) can be observed.

On the other hand, for points B-like and C-like, the photon polarization is not parallel to any of the sample's symmetry directions or planes, and the spectra have different symmetry mixtures depending on the measurement point in k -space (see also further).

From figure SF 3(c), we see then that at normal emission (point A) the two strongly dispersing parabolic bands are distinctly observed. These bands remain unchanged at points B and C [Figs SF 3(d,e)], though their spectral intensity decreases as the emission angle

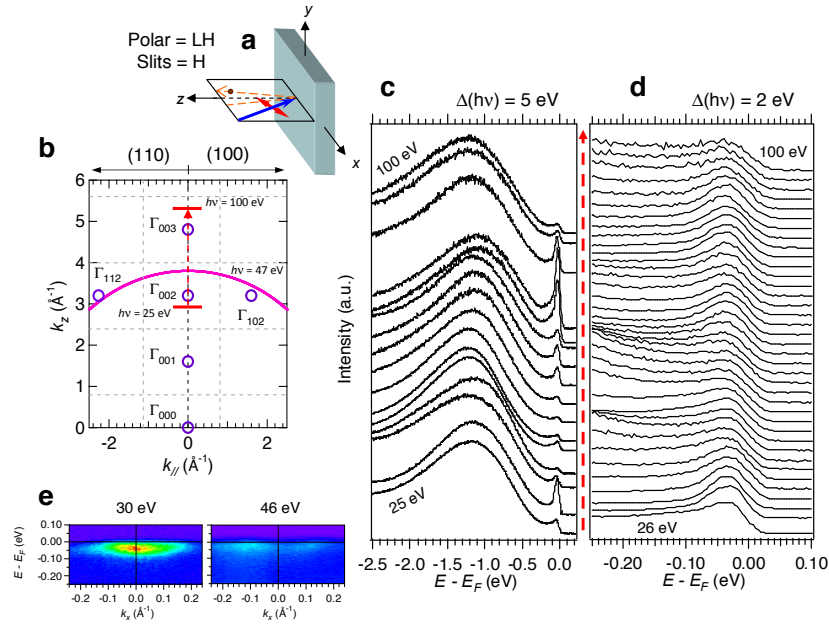


Figure SF 2: **Photon-energy dependence of the ARPES spectra of SrTiO₃.** **a**, Schematics of the experimental geometry for the data in this figure. The sample is the dark parallelepiped, the xz mirror plane is transparent, the light beam is represented by the blue arrow, its polarization by the red double arrow, and the collected electron beam by the dashed orange arrows. The same conventions are used in the rest of the figures in this Supplement. **b**, Representation of the 3D reciprocal space. The region covered by varying the photon energy from 25 eV to 100 eV is shown red dashed arrow and the thick red lines. The open circles are Γ points, the dashed lines are Brillouin-zone edges, and the violet circle is the spherical shell on which the measurements at $h\nu = 47$ eV are carried out. To convert the photon energy dependence into k_z dependence, an ‘inner potential’ of 12 eV was used, as deduced in previous works [SR10]. **c**, Integrated photoemission spectra at normal emission over a wide energy range, showing the oxygen-vacancy related intra-gap states at 1.3 eV [SR10] and the quasi-particle (QP) peak near E_F . Notice the large variations of the QP peak intensity as a function of photon energy (varying from 25 eV to 100 eV in steps of 5 eV). **d**, Zoom over the QP peak in c, after normalizing by the area of the peak. The peak does not disperse with photon energy (26 – 100 eV in steps of 2 eV), indicating its 2D character. **e**, Examples of two energy-momentum intensity maps at $h\nu = 30$ eV, at Γ_{002} , and $h\nu = 46$ eV, close to the zone edge. The band corresponds to the d_{xz} states. Its intensity is almost suppressed at $h\nu = 46$ eV, but the dispersion is unchanged.

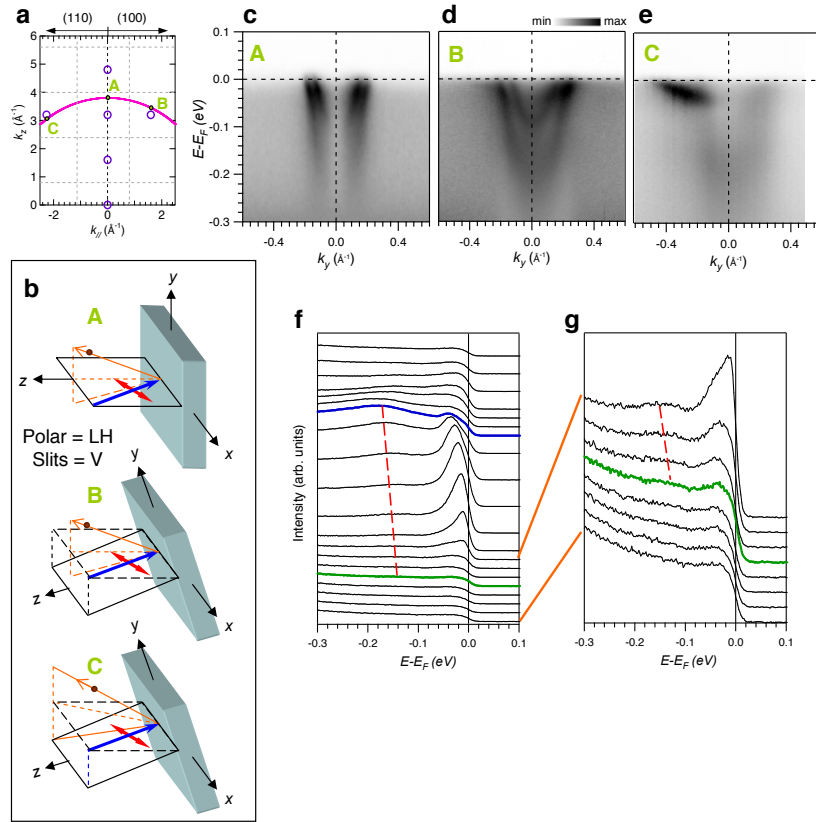


Figure SF 3: Intensity modulations of the electronic subbands as a function of emission angle. **a**, Schematic representation of the reciprocal space of SrTiO₃ over several Brillouin zones in the (100)–(001) and (110)–(001) planes. The continuous line is the spherical shell on which the measurements at $h\nu = 47$ eV are performed. **b**, Schematics of the experimental geometries for the data taken at points A, B and C in this figure. **c–e**, Energy-momentum intensity maps near E_F at points A, B and C represented in panel **a**. **f–g**, EDCs at point C integrated over intervals of 0.1 \AA^{-1} . The blue EDC is located at Γ , and the green EDC is at the zone edge

increases. Note, in particular, that although points B and C are equidistant from Γ , the light parabolic bands are more intense at point B, where the emission angle is lower. Conversely, the two weakly dispersing bands (the ‘upper and lower shallow bands’) are best seen at point C, where the emission angle is largest. Figures SF 3(f, g) show the energy distribution curves (EDCs) at point C integrated over intervals of 0.1 \AA^{-1} . The lower shallow band is clearly seen in the raw data dispersing from Γ (blue EDC) to the zone edge (green EDC).

Additionally, as noted in the main paper, the same asymmetric enhancement of the negative- k intensities for the two shallow bands is observed in point C. This indicates that the two shallow bands have the same symmetry. These shallow bands rapidly loose intensity as the emission angle decreases, to completely disappear in the spectra at normal emission, further indicating that their symmetry (or more generally, their spectral function) is not the same of either of the parabolic bands.

From the data of Fig. SF 3, it is then apparent that there is a unique underlying band structure at all three points A, B and C, further proving the 2D-like character of all the observed bands.

As described in the main text, the photoemission intensity from the different subbands is also strongly modulated by the photon polarization. For the sake of completeness in the discussion, we show again in Fig. SF 4 the energy-momentum intensity maps and EDCs taken at Γ_{102} (point B) for the non-doped sample. These data were collected at $h\nu = 45$ eV with V-slits (detection along y) using both LV and LH polarized photons, as shown in Figs. SF 4(a, b). In this geometry, where electrons are detected off-normal emission, only the xz -plane (coinciding with the light-incidence plane), where Γ_{102} lies, is a high-symmetry plane. For LV polarization, the light electric field is odd with respect to this mirror plane. Thus, only the d_{xy} - and d_{yz} -like bands, which are both odd with respect to the xz -plane, can be detected, as indeed observed [Figs. SF 4(c, d)]. On the other hand, for LH polarized light, the electric field is even with respect to the mirror plane, and only d_{xz} -like bands can be detected at Γ_{102} , also in agreement with the observation of the upper shallow band [Figs. SF 4(e, f)]. Away from Γ_{102} along the detection direction there is symmetry mixing. Experimentally, the lower parabolic band, but not the upper parabolic band, is again observed.

V. Band bending of the O-2p valence band

Figure SF 5(a) shows the angle-resolved data over a wide energy range at normal emission, LH polarization, V-slits and $h\nu = 47$ eV [point A in figure SF 4(a)] for the sample that has bulk doping $n_{3D} = 10^{18} \text{ cm}^{-3}$. The dispersion of the oxygen valence band, roughly located in between -9 eV and -4 eV, is clearly observed, attesting the high-quality of the surfaces obtained after cleaving. As seen from figures SF 5(a, b), the peak position of the valence-band maximum (VBM) is located at $E \approx -4.35$ eV, and the leading-edge of

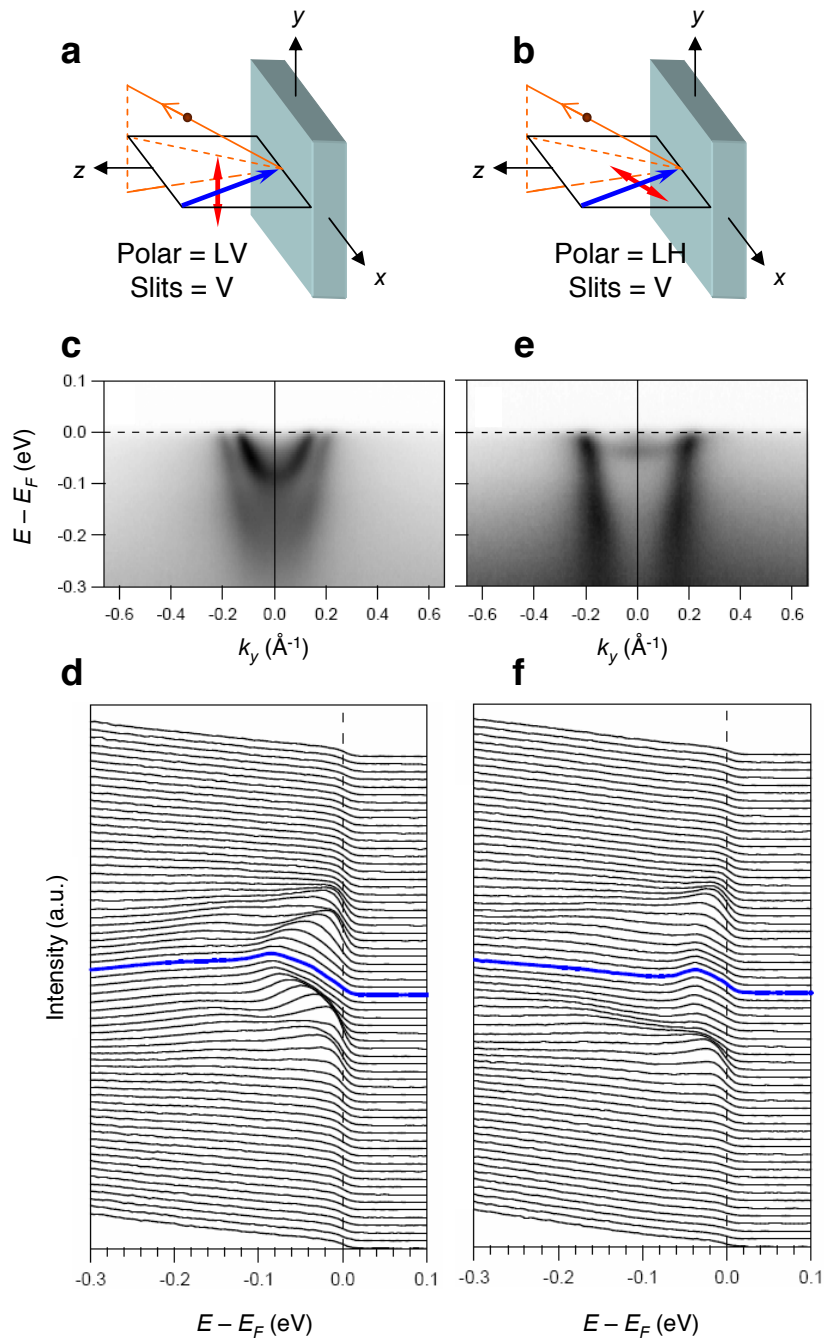


Figure SF 4: **Intensity modulations of the electronic subbands as a function of photon polarization.** **a, b**, Schematics of the experimental geometries for the data taken at point B [Fig. SF 3(a)] in this figure. **c, d**, Energy-momentum intensity map and EDCs for LV polarized light. **e, f**, Same measurements for LH polarized light. Blue EDCs are located at Γ_{102} . Both sets of spectra were obtained in the same spatial spot of the sample, at $T = 10$ K.

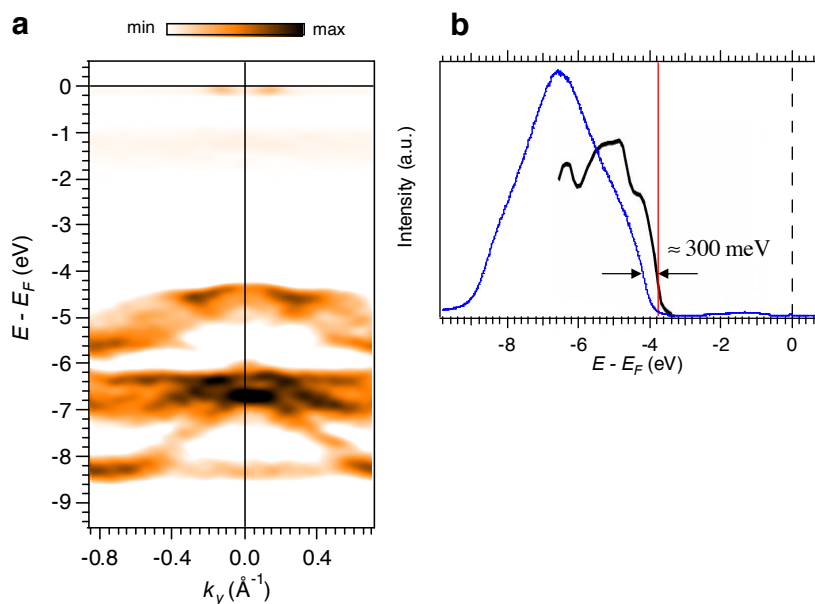


Figure SF 5: **ARPES spectra and band-bending of the O-2p valence band in SrTiO₃.** **a**, Second derivative of the energy-momentum intensity map over a wide energy range, showing the dispersion of the O-2p valence band at energies between 4–9 eV. The non dispersive oxygen-vacancy-induced intra-gap states at –1.3 eV, and the QP band at E_F , are also observed. **b**, Raw EDC at normal emission ($k_y = 0$) from the data in **a** (blue curve). The energy-dependent optical extinction coefficient measured in Ref. [SR14] is shown for comparison (black curve). The leading edge of the photoemission spectrum is shifted down by about 300 meV with respect to the optical absorption leading edge.

the valence band is located at about –3.9 eV. These values are systematically lower by 200-500 meV than the peak position of the bulk VBM, predicted to be about –3.9 eV by tight-binding calculations [SR12], and the bulk optical band gap of 3.75 eV [SR14], shown for comparison. These results are consistent with the dispersions and shifts reported in previous works [SR10, SR12]. More important, the observed energy down-shift of the oxygen valence band is in quantitative agreement with the confining potential at the surface, estimated to be $V_0 \approx -300$ meV (see below and main paper), and responsible for the formation of the two-dimensional electron gas and the subbands beneath the surface of cleaved SrTiO₃. This indicates that such a band shift of the O-2p valence band is due to band-bending by the above confining potential. Furthermore, as reported in the ultra-violet photoemission

experiments of Ref. [SR10], when the cleaved surface is exposed to oxygen, the O-2*p* valence band shifts back by about 200 meV towards E_F , and both the peak at -1.3 eV and the metallic quasi-particle peak at E_F (corresponding to our 2DEG) disappear –even though the sample is being irradiated to measure the photoemission spectrum. This lends support to the hypothesis that the confining potential and ensuing metallic 2DEG, in the case of cleaved SrTiO₃, are due to surface oxygen vacancies, rather than to (possibly persistent) photoconductivity as reported in *e.g.* LaAlO₃/SrTiO₃ interfaces [SR13].

VI. Wedge model

We approximate the effect of the confining potential acting in the z -direction by a potential wedge $V(z) = V_0 + eFz$, where e is the charge of the electron and F is the strength of the electric field along z . The quantized eigenenergies E_n are given in very good approximation by [SR15, SR16]:

$$E_n = V_0 + \left(\frac{\hbar^2}{2m_z^*} \right)^{1/3} \left[\left(\frac{3\pi}{2} \right) \left(n - \frac{1}{4} \right) eF \right]^{2/3}, \quad (1)$$

where $n = 1, 2, 3, \dots$, and m_z^* is the effective mass in the z -direction. The exact eigenenergies have $n - \frac{1}{4}$ in this equation replaced by 0.7587, 1.7540, and 2.7575, respectively, for the three lowest solutions [SR16]. The average value of z for the n -th subband is $eF \langle z_n \rangle = \frac{2}{3} |E_n - V_0|$ [SR16].

Replacing with the appropriate physical constants, one gets

$$E_n = V_0 + 9 \times 10^{-7} \left(\frac{m_e}{m_z^*} \right)^{1/3} \left(n - \frac{1}{4} \right)^{2/3} F^{2/3}, \quad (2)$$

where m_e is the free electron mass, E_n and V_0 are expressed in eV, and F is expressed in V/m. This expression allows to determine the field strength F from the experimental subband splitting $\Delta E = E_2 - E_1$ between the first to subbands of $d_{xz/yz}$ character. Notice that, in cubic symmetry, the d_{xz} - and d_{yz} -like bands have the same small effective mass in the z -direction, with $m_z^* \approx 0.7m_e$ from our experiments.

From the experimental value $\Delta E \approx 120$ meV, we get $F \approx 83$ MV/m.

Given the wedge-like form of the potential, the states with higher energy will have the largest extension along z . In our case, the observed highest occupied state is the upper shallow subband, which would correspond to the $n = 2$ state of the d_{xz} -like band. Thus, with the above field strength, we can estimate the depth (L) of the confining potential from

the approximation $eFL \approx [E_2(d_{xz}) - E_1(d_{xz})]$ (note that V_0 is not needed to compute this). This gives $L \approx 14.5 \text{ \AA}$, or about 3.7 unit cells.

The potential at the bottom of the wedge well (V_0) can, in turn, be estimated from the field strength and the bottom of the d_{xy} parabolic band [$E_1(d_{xy}) \approx -210 \text{ meV}$], which has a heavy mass along z of $m_z^* \approx 20m_e$. This yields $V_0 \approx -260 \text{ meV}$. This value allows an independent estimate of the width of the well from the average value of z for the $n = 2$ subband, namely $eF \langle z_2 \rangle = \frac{2}{3}|E_2 - V_0|$. Using $E_2(d_{xz}) = -40 \text{ meV}$, we obtain $\langle z_2 \rangle = 17.7 \text{ \AA}$, or about 4.5 unit cells. Additionally, as the potential $V(z)$ remains negative (*i.e.*, confining) while $eFz \lesssim V_0$, this yields $L_{max} \approx 31 \text{ \AA} \approx 8$ unit cells as a maximum bound for the width of the 2DEG. These independent estimates provide important crosschecks for the internal consistency of our analysis.

The energy of the bottom of the different $d_{yz/xz}$ subbands is then readily calculated from their light effective masses along z and the values of V_0 and F . One obtains: $E_1(d_{yz/xz}) = -100 \text{ meV}$, and $E_2(d_{yz/xz}) = +20 \text{ meV}$. This agrees with the observations: only the first d_{yz} subband (the small light parabola in the xy -plane) lies below E_F . The experimentally observed degeneracy lift between the d_{xz} and d_{yz} bands is not taken into account by this simple model. From the data, we know that the $E_1(d_{xz})$ subband (the lower shallow subband) is shifted by about 60 meV below its d_{yz} partner. One then expects that the upper shallow subband lies at an energy $E_2(d_{xz}) = E_2(d_{xz/yz}) - 60 \text{ meV} = -40 \text{ meV}$, again in excellent agreement with the observations.

Finally, we can also use our estimate of F to compute the superficial charge density σ_{2D} induced by the confining potential. We follow the same type of calculation used by Ueno and coworkers (Ref. [SR15], Supplementary Material), namely:

$$\frac{e}{2}\sigma_{2D} = \int_0^F \epsilon_0 \epsilon(F') dF', \quad (3)$$

where ϵ_0 is the vacuum dielectric constant and $\epsilon(F)$ is the material's dielectric permittivity. Empirically, it is well established that the dielectric permittivity of SrTiO_3 depends on the electric field strength F according to the relation [SR17]: $\epsilon(F) \approx 1/(4 \times 10^{-5} + 5 \times 10^{-10} F)$, where F is in V/m. We then readily obtain $\sigma \approx 0.25 e/a^2$, where $a = 3.905 \text{ \AA}$ is the cubic lattice parameter. This value is consistent with the experimental electron count 0.33 ± 0.03 electrons per a^2 , obtained from the area of the Fermi surfaces (see main text).

Note that in the above calculation we used the dielectric constant of bulk SrTiO_3 . But

in the region beneath the surface where the 2DEG establishes (about 5 unit cells) the solid has an electronic structure (hence a dielectric constant) that is different from that of the bulk. In other words, all the subbands of the 2DEG (including the filled one) contribute to the *dc* dielectric constant at the surface. The metallic subbands should contribute more to the screening than the filled band. Although our simple model does not allow us to quantify this, it is compatible with the fact that the calculated screening charge is lower but not too different from the experimental electron count.

Note further that the case of cleaved SrTiO₃ has an important difference from the LaAlO₃/SrTiO₃ interface. In the later, it is argued that there is a “polar catastrophe” creating a field that has to be screened. That field is screened by the electrons in all the available subbands. In contrast, in cleaved SrTiO₃, our results indicate that both the field and the electrons filling the 2DEG originate from oxygen vacancies, which are thus playing a double role. As a consequence, in cleaved SrTiO₃, the total count of electrons from the filled and partially filled subbands, which can be directly extracted from the ARPES data, corresponds to the electrons coming from all oxygen vacancies created in the spatial region occupied by the 2DEG (~ 5 unit cells). However, only the vacancies right at the surface will contribute to the electric field that confines the 2DEG. Those superficial vacancies are playing the role of the “polar interface here”. The estimate of these superficial vacancies is therefore not directly related to the total electron count.

VII. LDA slab calculations of the electronic structure in the presence of surface oxygen vacancies

To illustrate the effects on the band structure of SrTiO₃ due to the presence of oxygen vacancies near the surface, we performed *ab initio* density functional calculations within the local density approximation. We adopted the Wien2k code and modelled the surface by considering slabs of $1 \times 1 \times 12$ cells. We considered both SrO and TiO₂ terminations, and put one oxygen vacancy defect at the surface. Our goal here is to understand, through a realistic yet computationally simple calculation, whether the presence of such vacancies can yield a 2DEG at the surface with the concomitant energy lowering for the slab states. Thus, in this simple initial study, we considered the undistorted cubic cell and did not relax the lattice. Our results are presented in Fig. SF 6. They show that the main features of the

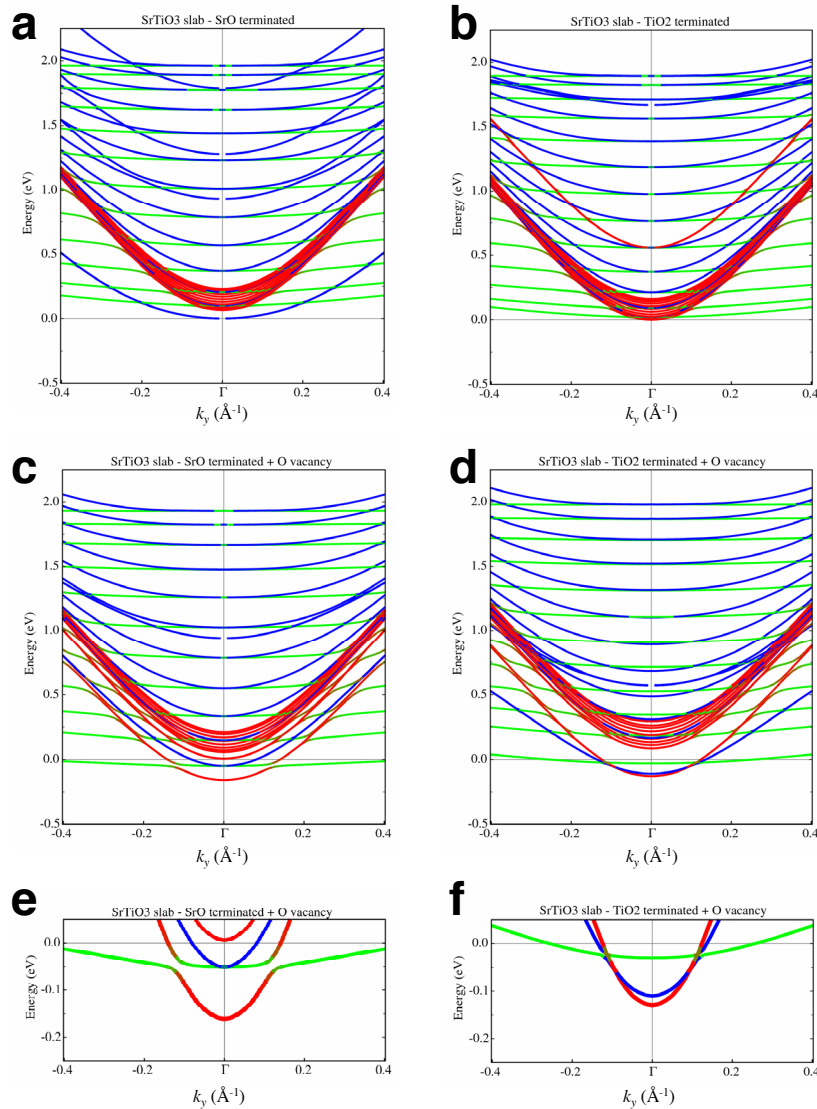


Figure SF 6: **Band structure calculation of $1 \times 1 \times 12$ slabs of cubic SrTiO_3 with one oxygen vacancy on the surface.** **a, b** Calculations for SrO and TiO_2 terminated surfaces, respectively. A subband structure of levels is created due to the z -direction confinement, with a large level spacing for the $d_{xz/yz}$ doublets, which share the same light mass m_z^* . In contrast the d_{xy} levels are hardly split due to their large m_z^* . Panels **c** and **d** include one oxygen vacancy defect at the SrO and TiO_2 surfaces. One clearly observes the double effect of doping and confinement. The bottom of the levels is pulled beneath the Fermi energy. Panels **e** and **f** show an enlarged detail of the energy region near E_F . Colors indicate the character of each band along k_y , following the same convention as in the main paper: d_{xy} -like bands are red, d_{yz} -like bands are blue, and d_{xz} -like bands are green.

2DEG at the surface of vacuum-cleaved SrTiO₃, discussed in the main text, are borne out by this calculation. Namely, that the bottom of the t_{2g} manifold around the Γ -point is lowered in energy by the effective attractive potential by as much as 200 meV. Moreover, the results also correctly capture the fact that the d_{xy} parabolic band, due to its large effective mass along the z -direction, is pulled down more than the $d_{xz/yz}$ doublet.

While it is appealing that these generic features are well captured by the LDA results, one should bear in mind that due to the technical limitations in the cell size that can be considered, our calculations remain on the qualitative level. A larger computational effort, including sub-superficial and clusters of surface vacancies, is in progress.

-
- [SR1] Chien, T. Y., Guisinger, N. P. & Freeland, J. W. Survey of fractured SrTiO₃ surfaces: From the micrometer to nanometer scale *J. Vac. Sci. Technol. B* **28**, C5A11-C5A13 (2010).
- [SR2] Guisinger, N. P. *et al.* Nanometer-scale striped surface terminations on fractured SrTiO₃ surfaces. *ACS NANO* **3**, 4132-4136 (2009).
- [SR3] Nakagawa, N., Hwang, H. Y. & Muller, D. A. Why some interfaces cannot be sharp. *Nature Mater.* **5**, 204-209 (2006).
- [SR4] van der Pauw, L. J. A Method of Measuring the Resistivity and Hall Coefficient on Lamellae of Arbitrary Shape, *Philips Technical Review* **20**, 220 (1958/59).
- [SR5] Tufte, O. N. & Chapman, P. W. Electron Mobility in Semiconducting Strontium Titanate, *Phys. Rev.* **155**, 796 (1967).
- [SR6] Frederikse, H. P. R. & Hosler, W. R. Hall Mobility in SrTiO₃, *Phys. Rev.* **161**, 822 (1967).
- [SR7] Louie, S. G. *et al.* Periodic oscillations of the frequency-dependent photoelectric cross sections of surface states: theory and experiment. *Phys. Rev. Lett.* **44**, 549-553 (1980).
- [SR8] Paggela, J. J., Miller, T. & Chiang, T. C. Angle-resolved photoemission from atomic-layer-resolved quantum well states in Ag/Fe(100). *J. Electron Spectrosc. Relat. Phenom.* **101-103**, 271-275 (1999).
- [SR9] Hüfner, S. Photoelectron spectroscopy: principles and applications. Third edition, Springer (2003).
- [SR10] Aiura, Y. *et al.* Photoemission study of the metallic state of lightly electron-doped SrTiO₃. *Surf. Sci.* **515**, 61 (2002).

- [SR11] Ishida, Y. *et al.* Coherent and Incoherent Excitations of Electron-Doped SrTiO₃. *Phys. Rev. Lett.* **100**, 056401 (2008).
- [SR12] Takizawa, M. *et al.* Angle-resolved photoemission study of Nb-doped SrTiO₃. *Phys. Rev. B* **79**, 113103 (2009).
- [SR13] Huijben, M. *et al.* Electronically coupled complementary interfaces between perovskite band insulators. *Nature Mater.* **5**, 556-560 (2006).
- [SR14] van Benthem, K., Elsässer, C. & French, R. H. Bulk electronic structure of SrTiO₃: experiment and theory. *J. Appl. Phys.* **90**, 6156 (2001).
- [SR15] Ueno, K. *et al.* Electric-field-induced superconductivity in an insulator. *Nature Mater.* **7**, 855-858 (2008).
- [SR16] Ando, T., Fowler, A. B. & Stern, F. Electronic properties of two-dimensional systems. *Rev. Mod. Phys.* **54**, 437-672 (1982).
- [SR17] Neville, R. C., Hoeneisen, B. & Mead, C. A. Permittivity of strontium titanate. *J. Appl. Phys.* **43**, 2124 (1972).